

On relative permeability data uncertainty and CO₂ injectivity estimation for brine aquifers

Simon A. Mathias^a, Jon G. Gluyas^a, Gerardo J. González Martínez de Miguel^{a,b}, Steven L. Bryant^c, David Wilson^b

^a*Department of Earth Sciences, Durham University, Durham, UK*

^b*ERC Equipoise Limited, London, UK*

^c*Department of Petroleum and Geosystems Engineering, University of Texas at Austin, US*

Abstract

Performance assessment of possible CO₂ storage schemes is often investigated through numerical simulation of the CO₂ injection process. An important criterion of interest is the maximum sustainable injection rate. Relevant numerical models generally employ a multi-phase extension to Darcy's law, requiring data concerning the evolution of relative permeability for CO₂ and brine mixtures with increasing CO₂ saturation. Relative permeability data is acutely scarce for many geographical regions of concern and often cited as a major source of uncertainty. However, such data is expensive and time consuming to acquire. With a view to improving our understanding concerning the significance of relative permeability uncertainty on injectivity, this article presents a sensitivity analysis of sustainable CO₂ injection rate with respect to permeability, porosity and relative permeability. Based on available relative permeability data obtained from 25 sandstone and carbonate cores discussed in the literature, injectivity uncertainty associated with relative permeability is found to be as high as $\pm 57\%$ for open aquifers and low permeability closed aquifers (< 50 mD). However, for high permeability closed aquifers (> 100 mD), aquifer compressibility plays a more important role and the uncertainty due to relative permeability is found to reduce to $\pm 6\%$.

Key words: Relative permeability, Geologic carbon sequestration, Pressure buildup

1. Introduction

There has been much effort focused on estimating volumetric CO₂ storage capacity in brine aquifers over large regional areas in many different countries. However, there is an increasing

Preprint submitted to International Journal of Greenhouse Gas Control *September 18, 2012*

28 understanding that such estimates are of limited value if not attached to some form of associated
29 economic cost of utilization (Allinson et al., 2010). A major geologically dependent factor in this
30 respect is the number of injection wells needed to utilize the storage capacity within a practical
31 amount of time (Ehlig-Economides and Economides, 2010), which, in effect, is a measure of what
32 many researchers refer to as injectivity.

33 Injectivity is dependent on many reservoir specific parameters, including permeability, poros-
34 ity, formation thickness, areal extent, pressure, temperature, brine salinity and relative permeability
35 (Mathias et al., 2011a). For regions with historic and contemporary oil and gas industries, esti-
36 mates for these parameters are already available in national and corporate databases (e.g. Wilkin-
37 son et al., 2011). The exception to this are those parameters associated with CO₂-brine relative
38 permeability, the reason being that (1) it has not been historically of interest to collect such infor-
39 mation and (2) it is very expensive and time-consuming to obtain (Muller, 2011). Consequently,
40 researchers are generally restricted to using data from the literature, often associated with different
41 geological environments (e.g. Dria et al., 1993; Bennion and Bachu, 2008; Perrin and Benson,
42 2010; Pickup et al., 2011; Krevor et al., 2012).

43 In a recent study, Burton et al. (2009) found that uncertainty in relative permeability data can
44 lead to a four-fold variation in injectivity. Specifically, Burton et al. (2009) estimated maximum
45 sustainable injection rates using an approximate equation for predicting pressure build-up due to
46 CO₂ injection into a brine aquifer (Burton et al., 2008). All parameters were held constant, in-
47 cluding permeability and porosity, except for those associated with relative permeability. They
48 repeated the simulations using relative permeability parameter sets from seven different core-flood
49 experiments (reported previously by Bennion and Bachu, 2008). However, the nature of the sim-
50 plifying assumptions used by Burton et al. (2009) may have overemphasized this point. Their
51 approximate solution assumes fixed pressure boundaries at both the injection well face and the
52 far-field boundary and that both the brine and CO₂ are incompressible. Consequently, at the start
53 of injection, the pressure profile corresponds to one that would be expected for steady state injec-
54 tion of brine (with the same constant injection pressure). As CO₂ is introduced, the CO₂ injection
55 rate increases as a consequence of an increase in bulk mobility associated with the lower viscos-
56 ity of CO₂ (as compared to brine). The main control on this change in mobility are the relative

57 permeability parameters.

58 If instead an initially uniform pressure distribution is considered, at the start of injection there
59 is a spatial step change in pressure from the injection well to the boundary of the aquifer. With
60 time, this pressure front moves out and becomes more attenuated. The migration of the pressure
61 wave is controlled by the intrinsic permeability of the formation and the bulk compressibility of
62 the reservoir fluid and formation. Such a scenario predicts CO₂ injection rate to be highest at the
63 beginning of the simulation. With time, as the pressure gradients reduce, in contrast to the Burton
64 et al. (2009) study, there will be a corresponding reduction in CO₂ injection rate (for the constant
65 injection well pressure scenario). For this more realistic scenario, it can be imagined that intrinsic
66 permeability and compressibility play will play a more important role on injectivity.

67 More recently, Mathias et al. (2011b) derived a semi-analytical solution for pressure buildup
68 due to constant rate of CO₂ injection into a closed brine aquifer with an initially uniform pressure
69 distribution. Their model extends work previously presented by Mathias et al. (2009) and Mathias
70 et al. (2011a) by allowing for non-linear relative permeability and partial miscibility between the
71 CO₂ and brine. In this study, following the idea of Burton et al. (2009), the role of relative perme-
72 ability is studied by simulating CO₂ injection into formations of various permeabilities, porosities,
73 radial extents of aquifer, reservoir conditions and brine salinities with each scenario repeated for
74 25 different relative permeability parameter sets for sandstone and carbonate formations currently
75 available from the literature (Bennion and Bachu, 2008; Perrin and Benson, 2010; Krevor et al.,
76 2012).

77 The structure of this article is as follows: Firstly, the relative permeability data sets selected
78 from the literature are discussed. Relevant results from numerical simulation, using TOUGH2
79 (Pruess et al., 1999) with ECO2N (Pruess, 2005; Pruess and Spycher, 2007), of the CO₂ injection
80 problem are presented. The accuracy of the aforementioned semi-analytical solution for non-
81 linear relative permeabilities is verified by comparison with simulation output from the numerical
82 simulator. Discussion is given with regards to parameterizing permeability reduction due to salt
83 precipitation. Results from a sensitivity analysis, using the pressure buildup equation of Mathias
84 et al. (2011b), are then presented and discussed.

2. Relative permeability data

Relative permeability characteristics are often represented in numerical and mathematical reservoir simulators by power laws of the form (e.g. Orr, 2007):

$$k_{ra} = k_{ra0} \left(\frac{1 - S_g - S_{ar}}{1 - S_{gc} - S_{ar}} \right)^m \quad (1)$$

$$k_{rg} = k_{rg0} \left(\frac{S_g - S_{gc}}{1 - S_{gc} - S_{ar}} \right)^n \quad (2)$$

where k_{ra} [-] and k_{rg} [-] are the relative permeabilities for the aqueous and CO₂ rich phases, respectively (hereafter, referred to, for convenience, as the aqueous and gas phase, respectively), S_g [-] is the gas phase volumetric saturation (i.e., the volumetric proportion of pore-space occupied by CO₂ rich phase), S_{ar} [-] is the residual aqueous phase saturation, S_{gc} [-] is the critical gas saturation, and k_{ra0} [-], k_{rg0} [-], m [-] and n [-] are the end-point relative permeabilities and power-law exponents for the aqueous and gas phases, respectively.

Bennion and Bachu (2008, 2010) present parameters for Eqs. (1) and (2) for a range of sandstone, carbonate and cap-rock formations from Alberta, Canada. These data were obtained from transient drainage and imbibition experiments for CO₂-brine mixtures at various reservoir conditions. Rather than deriving values of relative permeability for specific values of saturation, such as is often done with variations of the so-called JBN method (Johnson et al., 1959), Bennion and Bachu (2008, 2010) use a history matching technique similar to that described by Sigmund and McCaffery (1979). In this way, the relative permeability parameters for Eqs. (1) and (2) are derived directly from the pressure buildup and fluid recovery data measured during the experiments.

The various formations were studied at a range of different pressures, temperatures and salinities so as to better represent their associated in situ environments. Pressure, temperature and salinity mostly affect relative permeability through the interfacial tension (IFT) that develops between the brine and CO₂. High IFT tends to lead to greater non-linearity between relative permeability and fluid saturation (Bachu and Bennion, 2008). Permeability, porosity, IFT and relative permeability parameter values (for Eqs. (1) and (2)) are summarized for the Bennion and Bachu (2008, 2010) drainage experiments on sandstone and carbonate cores in Table 1. Note that Bennion and

110 Bachu (2008, 2010) assumed $k_{ra0} = 1$ and $S_{gc} = 0$ for all the drainage experiments.

111 Perrin and Benson (2010) obtained relative permeability data for a heterogenous sandstone
112 core provided by the CO2CRC-Otway project and a more homogenous Berea sandstone core.
113 For both cases, relative permeability data was obtained by performing a sequence of steady-state
114 drainage experiments, under reservoir conditions, whereby initially brine saturated cores were
115 injected with CO₂-brine mixtures of sequentially increasing CO₂ content. Volume averaged CO₂
116 saturations of the cores were measured using an X-ray CAT scanner. The final results took the
117 form of a set of discrete relative permeability and CO₂ saturation data for each of the steady-state
118 saturations achieved.

119 Krevor et al. (2012) used a similar method to Perrin and Benson (2010) and obtained relative
120 permeability data for four more sandstone cores including Berea Sandstone, Paaratte Formation
121 (also from Otway, Australia), Mt. Simon Formation (Illinois, US) and Tuscaloosa Formation (from
122 the Cranfield CO₂ injection site, Mississippi, US).

123 To aid comparison of the Perrin and Benson (2010) and Krevor et al. (2012) data with that
124 from Bennion and Bachu (2008, 2010), we have obtained corresponding parameters for Eqs. (1)
125 and (2) by least-squares fitting to the data given in Figs. 9 and 13 of Perrin and Benson (2010) and
126 Fig. 13 of Krevor et al. (2012). These are additionally summarized alongside associated values of
127 permeability, porosity and IFT in Table 1. To be consistent with Bennion and Bachu (2008, 2010),
128 we uniformly assumed $k_{ra0} = 1$ and $S_{gc} = 0$ (this was found to have very little impact on goodness
129 of fit with the data). Note that Krevor et al. (2012) provided parameter fits for Brooks-Corey
130 relations, which are different to the expressions given in Eqs. (1) and (2).

131 The relative permeability curves for all 25 parameter sets are plotted in Fig. 1. The sandstones
132 are shown in Figs. 1a and b whilst the carbonates are shown in Figs. 1c and d. There is a very
133 wide range of different responses. There are no obvious differences between the sandstone and
134 carbonate formations. Even for repeat runs on the same formations, there are wide variations
135 in both non-linearity and end-point relative permeability (e.g. Berea #1 and #2). There is also
136 little difference between results obtained using steady-state and transient experimental methods
137 (compare Figs. 1a and b). Note that both methods yielded low (e.g. Tuscaloosa and Ellerslie) and
138 high (e.g. Otway and Cardium #1) end-point relative permeabilities. See Muller (2011) for further

139 discussion on the differences between these two methods.

140 **3. Simulation of CO₂ injection in brine aquifers**

141 It is clear from Table 1 and Fig. 1 that a wide range of relative permeability characteristics can
142 be expected from reservoir rocks of interest in the future. As stated earlier, to better understand the
143 importance of this uncertainty on CO₂ injectivity, here we consider the semi-analytical pressure
144 buildup equation recently presented by Mathias et al. (2011b).

145 The equation predicts pressure buildup as a consequence of a constant mass injection rate of
146 CO₂ into a closed or open brine aquifer. Building heavily on the work of Nordbotten et al. (2005),
147 Orr (2007), Zeidouni et al. (2009) and Mathias et al. (2009, 2011a), derivation of the equation
148 involves invoking of a number of simplifying assumptions including:

- 149 1. Vertical pressure equilibrium;
- 150 2. Negligible capillary pressure;
- 151 3. Constant fluid properties;
- 152 4. Homogenous, isotropic and cylindrical aquifer formation;
- 153 5. Constant mass injection rate through a centrally located fully completed vertical well;
- 154 6. Formation is confined above and below (lateral confinement is optional).

155 From comparison with isothermal simulations from TOUGH2, Mathias et al. (2009, 2011a)
156 found the first three assumptions not to be important for pressure buildup providing an appropriate
157 reference pressure is used to estimate the constant CO₂ fluid properties. However, all the simula-
158 tions studied assumed linear relative permeability functions. Therefore, to further test the validity
159 of the semi-analytical solution, additional TOUGH2 (Pruess et al., 1999) simulations, with the
160 equation of state module, ECO2N (Pruess, 2005; Pruess and Spycher, 2007), were performed with
161 increasingly non-linear relative permeability.

162 The ECO2N module provides a number of different relative permeability functions that can be
163 chosen. However, to be consistent with the CO₂ and brine relative permeability data sets given in
164 Table 1, we implemented the equations given in Eqs. (1) and (2). As within the studies of Mathias

165 et al. (2011a), gas saturation was assumed to be related to capillary pressure, P_c [$\text{ML}^{-1}\text{T}^{-2}$], via
 166 the van Genuchten (1980) function

$$\frac{1 - S_g - S_{ar}}{1 - S_{gc} - S_{ar}} = \left(1 + \left|\frac{P_c}{P_{c0}}\right|^{n_v}\right)^{-m_v}, \quad n_v = \frac{1}{1 - m_v} \quad (3)$$

167 where m_v [-] is another empirical parameter. The parameters P_{c0} [$\text{ML}^{-1}\text{T}^{-2}$] and m_v [-] are empiri-
 168 cal parameters taken to be the same values as those used in the saline aquifer studies of Zhou et al.
 169 (2008).

170 To study the effect of non-linearity, a scenario similar to Scenario c) presented by Mathias et
 171 al. (2011a) was simulated with different values of m with $m = n$ (recall that Mathias et al. (2011a)
 172 only studied the linear relative permeability case when $m = n = 1$). The full set of parameters
 173 used are listed in Table 2.

174 All the simulations assumed vertical pressure equilibrium and were setup as one-dimensional
 175 axially symmetric problems. See Mathias et al. (2011a,b) for further discussion concerning vertical
 176 pressure equilibrium in this context. Following Mathias et al. (2009), the location of the discretized
 177 points in space were distributed logarithmically to ensure higher resolution at the injection well.

178 Fig. 2a compares well pressures from the semi-analytical solution (the solid lines) with those
 179 from TOUGH2 (the circular markers). The results from the semi-analytical solution were obtained
 180 by assuming a pressure of 18 MPa for the constant fluid properties. Fluid properties for CO_2 and
 181 brine mixtures were estimated using MATLAB implementations of equations presented by Batzle
 182 and Wang (1992), Spycher et al. (2003); Spycher and Pruess (2005) and Fenghour et al. (1998).

183 Both the semi-analytical solution and TOUGH2 predict pressure to rise monotonically with
 184 time. Increasing the non-linearity of the relative permeability functions (i.e., increasing m) leads to
 185 an almost constant increase in pressure. The plots confirm that the close correspondence between
 186 well pressures from the semi-analytical solution and TOUGH2 is not diminished with increasingly
 187 non-linear relative permeability functions.

188 At this point it is also interesting to re-examine Burton et al. (2008)'s approximation. Burton
 189 et al. (2008, 2009) avoid numerical integration by assuming uniform relative permeabilities within
 190 the two-phase region based on the arithmetic mean of the CO_2 saturation at the trailing and leading

191 shock fronts. In this way, it is assumed that (referring explicitly to Eq. (58) of Mathias et al.
 192 (2011b))

$$F_2(z) = \frac{1}{\mu_g} \int_z^{z_L} \left(\frac{k_{ra}}{\mu_a} + \frac{k_{rg}}{\mu_g} \right)^{-1} \frac{1}{z} dz \approx \frac{1}{\mu_g} \left(\frac{k_{ra}}{\mu_a} + \frac{k_{rg}}{\mu_g} \right)^{-1}_{S_g=(S_{gT}+S_{gL})/2} \ln\left(\frac{z_L}{z}\right) \quad (4)$$

193 where z is a similarity transform found from

$$z = \frac{\pi\phi\rho_c H r^2}{M_0 t} \quad (5)$$

194 and μ_a [$\text{ML}^{-1}\text{T}^{-1}$] and μ_g [$\text{ML}^{-1}\text{T}^{-1}$] are the dynamic viscosities of the aqueous and gas phase,
 195 respectively, z_L is the value of z at the front of the CO_2 plume (i.e., the location of the leading
 196 shock), ϕ [-] is porosity, ρ_c [ML^{-3}] is the density of pure CO_2 , H [L] is formation thickness, r [L]
 197 is radial distance from the well, M_0 [MT^{-1}] is mass injection rate of CO_2 and t [T] is time after
 198 start of injection.

199 However, it is still necessary to find the locations of the shock fronts by iterative solution of
 200 Eq. (30) of Mathias et al. (2011b). Results for well pressures using Burton's approximation are
 201 plotted as dashed lines in Fig. 2a alongside those from the TOUGH2 simulation and the semi-
 202 analytical solution. Well pressures predicted using Burton's approximation tend to overestimate
 203 those from the semi-analytical solution and TOUGH2. However, this error appears to decrease
 204 with increasingly non-linear relative permeability functions.

205 Profile plots of gas saturation and pressure against radial distance for various times, obtained
 206 using TOUGH2 (circular markers), the semi-analytical solution (solid lines) and Burton's approx-
 207 imation (dashed lines), are plotted for the $m = 3$ case in Figs. 2b and c, respectively. Again, the
 208 close correspondence between TOUGH2 and the semi-analytical solution is undiminished. Note
 209 that Burton's approximation gives rise to a linear-log pressure profile in the two-phase region,
 210 which closely follows that from TOUGH2 and the numerically integrated semi-analytical solu-
 211 tion. Clearly Burton's method is a useful alternative to numerically evaluating the integral in Eq.
 212 (4). However, if one is in a position to iteratively solve Eq. (30) of Mathias et al. (2011b), accurate
 213 numerical integration of Eq. (58) of Mathias et al. (2011b) is quite a trivial extra step.

214 Iterative solution of Eq. (30) of Mathias et al. (2011b), for the shock front locations, was

215 achieved using MATLAB's optimization routine, FMINSEARCH. Numerical integration of Eq.
216 (58) of Mathias et al. (2011b) was achieved using the trapezoidal method (via MATLAB's TRAPZ
217 function) with z values obtained from a corresponding vector of 200 equally spaced values of S_g
218 between S_{gL} and S_{gT} . Results shown for when $m = n = 1$ were obtained from the closed-form
219 equations for this special case, also given in Mathias et al. (2011b). It is demonstrated here that the
220 numerically integrated semi-analytical solution of Mathias et al. (2011b) is an accurate alternative
221 to TOUGH2 ECO2N for the non-linear relative permeability simulation scenarios considered.
222 In the following sections, the semi-analytical solution is used to explore the role of uncertainty
223 concerning relative permeability on pressure-buildup by sensitivity analysis.

224 Recall that the well pressures plotted in Fig. 2a are all monotonically increasing with time.
225 Numerically simulated constant rate CO₂ injections are often reported to lead to non-monotonic
226 well pressure behavior in the form of an early-time pressure spike (e.g. Zhou et al., 2008; Chad-
227 wick et al., 2009; Okwen et al., 2011). Indeed, we have also observed a spike in pressure at early
228 times from simulations undertaken using TOUGH2, ECLIPSE-100 and CMG-GEM. However, on
229 increasing the grid resolution around well it is found that the pressure spike decreases in duration.
230 Furthermore, once sufficient grid resolution is realized, the pressure spike ultimately vanishes, in
231 accordance with the monotonic results predicted by the semi-analytical solution. Similar results
232 are also reported by Pickup et al. (2012). The grid used to obtain the results given in Fig. 2 em-
233 ployed 451 logarithmically spaced points with the first element (next to the well) being of 1 mm
234 length.

235 **4. Permeability reduction due to salt precipitation**

236 In the previous section, the permeability reduction factor due to salt precipitation, k_{rs} [-], was
237 set to one throughout (i.e., it was assumed that salt precipitation led to no permeability reduction).
238 To incorporate the effect of salt precipitation on permeability reduction in our subsequent analysis,
239 we have employed the experimental data obtained by Bacci et al. (2011) for a St Bees sandstone
240 core (Fig. 3).

241 Previous researchers have used the Verma and Pruess (1989) model for this purpose, commonly
242 with the so-called Γ and ϕ_r parameters somewhat arbitrarily set to 0.8 (after Pruess et al., 1999).

243 Through least-squares fitting we found $\Gamma = \phi_r = 0.57$ leads to a good fit to the experimental data
244 (see Fig. 3). However, a better fit is obtained by linear regression of the power law

$$k_{rs} = \frac{k}{k_0} = \left(\frac{\phi}{\phi_0} \right)^\eta \quad (6)$$

245 where k [L^2], k_0 [L^2], ϕ [-], ϕ_0 [-] are current permeability, initial permeability, current porosity
246 and initial porosity, respectively and η [-] is an empirical exponent. Linear regression yields an η
247 value of 5.74 (see Fig. 3). Note that $\phi/\phi_0 = 1 - S_s$ where S_s [-] is the volumetric saturation of
248 participated salt (see Eq. (38) of Mathias et al., 2011b). For the remainder of the analysis, k_{rs} is
249 calculated from Eq. (6) with $\eta = 5.74$.

250 Kim et al. (2012) usefully distinguish between non-localized and localized salt precipitation.
251 Non-localized salt precipitation is characterized by uniform salt precipitation within the dry-out
252 zone, which largely comes about due to vaporization of residually trapped brine. Localized salt
253 precipitation is characterized by an abnormally high level of salt precipitation at the dry-out front,
254 where strong capillary forces cause displaced brine to re-imbibe back towards the well.

255 Recall that the semi-analytical solution, discussed in the previous section, ignores capillary
256 forces. Consequently, this localized salt precipitation is unaccounted for in the analysis described
257 in this paper. However, capillary driven back flow is likely to reduce with increasing injection
258 rate. Interestingly, comparing results from models which ignored and included capillary pressure
259 (and in turn, counter current imbibition), Pruess and Muller (2009) found that inclusion of capil-
260 lary pressure effects is unlikely to increase salt precipitation by more than a factor of order 1.1.
261 Furthermore, notable changes in the shape of the dry-out zone, as a result of counter current im-
262 bibition, were only observed for the exceptionally small injection rate of 0.025 kg/s/m per unit
263 length of fully completed vertically orientated well screen (see their Fig. 7). It is expected that
264 accounting for localized salt precipitation would not lead to significant differences in conclusions
265 to the analysis described in our article.

5. Dimensionless pressure buildup contribution due to relative permeability

Pressure buildup due to CO₂ injection in brine aquifers is dependent on many characteristics in addition to relative permeability, in particular, reservoir volume, porosity, permeability and injection duration. However, it is possible to separate out these effects by simple manipulation of the equations presented by Mathias et al. (2011b). Recall in Fig. 2a that increasing the relative permeability non-linearity led to a relatively constant increase in pressure. Inspection of Eq. (57) of Mathias et al. (2011b) reveals that for large time, almost all of the relative permeability characteristics within the pressure buildup equation takes the form of the following dimensionless constant, P_{rpD} [-], found from

$$P_{rpD} = \frac{1}{\mu_c} \left[\frac{\mu_c}{k_{rs}} \ln z_T + \mu_g q_{D2} F_2(z_T) - \mu_b q_{D3} \ln z_L \right] \quad (7)$$

where μ_c [ML⁻¹T⁻¹] and μ_b [ML⁻¹T⁻¹] are the dynamic viscosities of pure CO₂ and CO₂-free-brine, respectively, F_2 is found from the integral form of Eq. (4), z_T is the value of z at the edge of the dry-out zone (that develops around the well due to brine vaporization) and q_{D2} [-] and q_{D3} [-] are dimensionless volumetric flow reductions due to brine vaporization and CO₂ dissolution, respectively. Note that z_T and z_L are both constants.

Calculation of all the terms given in Eq. (7) require additional auxiliary functions described in detail by Mathias et al. (2011b). But the important point to note is that, given an equation of state for the CO₂-brine mixture, $P_{rpD} = f(P_{ref}, T, \omega_{sb}, S_{ar}, S_{gc}, k_{ra0}, k_{rg0}, k_{rs}, m, n)$, where P_{ref} [ML⁻¹T⁻²], T [θ], ω_{sb} [-] are the reference pressure, temperature and salt mass fraction in brine needed for calculation of the various relevant fluid properties. Therefore for a given set of reservoir conditions (P_{ref}, T, ω_{sb}), it is possible to assess the relative significance of the 25 relative permeability parameter sets given in Table 1 by the constant values provided by Eq. (7).

Values of P_{rpD} were calculated for the 25 parameter set, assuming $P_{ref} = 15$ MPa, $T = 40$ °C and $\omega_{sb} = 0.15$. Each value is plotted against k_{rg0} , S_{ar} , m and n in Figure 4. It can be seen that there are a wide range of P_{rpD} values from close to zero up to 221. The largest P_{rpD} values correspond with the smaller k_{rg0} values. The smallest P_{rpD} values correspond with those values of brine exponent, m , closest to unity (i.e., approaching linear brine relative permeability). There is

292 also some tendency of P_{rpD} increasing with S_{ar} , presumably because larger values of S_{ar} tend to
293 correspond with smaller values of k_{rg0} . There seems to be no obvious trend with the CO₂ exponent,
294 n , and there is little difference between the response of the sandstone and carbonate cores. The
295 largest P_{rpD} value is attributable to the Tuscaloosa formation. Although Tuscaloosa does not have
296 the smallest k_{rg0} , it has moderate to large values for S_{ar} , m and n . The value of P_{rpD} is not strongly
297 dependent on any single parameter, rather it is controlled by the combined parameter set as a
298 whole.

299 Fig. 5 shows a plot of porosity against permeability for the 25 parameter sets. As is normally
300 observed, larger porosities tend to lead to larger permeabilities. Bachu and Bennion (2008) ob-
301 served a good correlation between permeability and k_{rg0} , although only after excluding one of 13
302 rock samples. Fig. 6 shows plots of k_{rg0} , S_{ar} , m , n and P_{rpD} against porosity, permeability and
303 IFT for all 25 parameter sets. Again, there is no obvious difference between the sandstone and
304 carbonate cores. Contrary to Bachu and Bennion (2008), Fig. 6f shows no link between k_{rg0} and
305 permeability. There is an interesting pattern between m and ϕ in Fig. 6c, but only for $\phi > 15\%$.
306 But more importantly, for the 25 parameter sets studied, there is no apparent link between P_{rpD}
307 and lithology, permeability, porosity and/or IFT (see Figs. 6 e, j and o).

308 6. Injectivity sensitivity analysis

309 From Figs. 6e, j and o it can be concluded that: (1) the 25 relative permeability parameter sets
310 (RPPS) given in Table 1 are likely to lead to a wide range of injectivities; (2) there is no apparent
311 link between lithology, porosity, permeability and/or IFT with relative permeability. It is therefore
312 interesting to propagate the uncertainty associated with the 25 RRPS (i.e., k_{rg0} , S_{ar} , m , n) through
313 to injectivity for a range of practical dimensional scenarios of interest.

314 Consider the base case described in Table 3. Figs. 7a to d show pressure responses predicted
315 by the semi-analytical solution using the 25 RPPS. Maximum sustainable injection rates for each
316 RPPS were obtained by iteration such that the well pressure equals P_{max} after 30 years. The
317 individual injection rates are detailed in the legends given in Figs. 7a to d. Note that this analysis
318 ignores the porosity and permeability data given in Table 3 and uses only the RPPS (i.e., k_{rg0} , S_{ar} ,
319 m , n).

320 Not surprisingly (given the discussion in the previous section), the Tuscaloosa Sandstone yields
321 the lowest injection rate at 5.4 kg/s. The largest injection rate is achieved using the Slave Point
322 Carbonate at 13.1 kg/s. Therefore, for the scenario depicted by the parameters given in Table 3,
323 uncertainty concerning RPPS has led to a 2.4-fold variation in injection. Recall that Burton et al.
324 (2009) observed a 4-fold variation in injectivity for their considered scenario. Limiting the study
325 to the cores studied by Burton et al. (2009) (Wabamun #1, Basal Cambrian, Wabamun #2, Nisku
326 #1, Viking #1, Ellerslie, Cooking Lake #1), the minimum and maximum injection rates are 9.4
327 kg/s and 12.1 kg/s from Ellerslie and Wabamun #1, respectively, leading to a 1.3-fold variation.

328 As discussed in the introduction, the analysis of Burton et al. (2009) ignores the compressibility
329 of the aquifer. In this case, the amount of CO₂ that can be injected into the aquifer is dependent
330 only on the RPPS and the permeability of the aquifer. For the compressible closed aquifer scenario,
331 represented by the parameters in Table 3, compressibility plays an additional role on injectivity and
332 hence the importance of uncertainty in RPPS is reduced.

333 Fig. 8a shows plots of maximum sustainable injection rate for each of the 25 RPPS for the
334 base case described in Table 3 but for different reservoir permeabilities and porosities, as indicated
335 by the x-axis and legend, respectively. For small permeabilities, results for the three porosities
336 converge as injection capacity becomes permeability limited and independent of available pore-
337 volume. For large permeabilities, injection capacity flattens off with permeability and there is
338 a greater variation with porosity. This can be explained as follows: For small injection rates
339 (associated with small permeabilities), the associated pressure wave does not have time reach the
340 outer boundary of the aquifer, during the 30 year period studied. Hence for small injection rates,
341 the reservoir units are insensitive to the total available pore-volume and are acting as would be
342 expected for infinite units (consider Eq. (59) of Mathias et al. (2011b)). For larger injection rates
343 (associated with large permeabilities), the associated pressure wave reaches the outer boundary
344 of the aquifer during the 30 year period. In this case, the reservoir units become less sensitive to
345 permeability and more dependent on the bulk aquifer compressibility.

346 For the range of permeabilities and porosities studied, injectivity variation associated with
347 uncertainty in relative permeability is a fraction of that for permeability and porosity. Note that
348 the minimum and maximum injection rates are due to the Tuscaloosa Sandstone and Slave Point

349 Carbonate, respectively.

350 The black solid and dashed lines in Fig. 8a are the mean and mean \pm two standard deviations
351 (which for normally distributed data corresponds to the 50, 97.7 and 2.3 percentiles, respectively)
352 of injection rates for 25 RPPS. Interestingly, it is the Ellerslie sandstone (highlighted in yellow)
353 that most closely follows the mean response. Furthermore, if one wanted to use linear permeability
354 functions (i.e., $m = n = 1$, so as to benefit from the closed-form expressions for the locations of
355 the two shock fronts given by Mathias et al. (2011b)) it is found that $k_{rg0} = 0.1$ and $S_{ar} = 0.2$ gives
356 a good approximation to the mean response (the white circular markers).

357 Fig. 8b shows an equivalent plot of percentage variation in injection rate (PVIR) associated
358 with the 25 RPPS, obtained by dividing two standard deviations by the mean and multiplying by
359 100. Independent of porosity, the PVIR = 47% for low permeabilities ($k \ll 100$ mD). However,
360 with increasing permeability, the PVIR decreases to between 7% and 13%.

361 Fig. 9 shows plots of mean and \pm two standard deviations for the base case scenario but
362 with a), b), c) and d) looking at sensitivity to aquifer size, injection duration, reservoir conditions
363 and formation water salinity, respectively. Maximum sustainable injection rate is seen to increase
364 with increasing aquifer size, decreasing injection duration, increasing aquifer depth (assuming hy-
365 drostatic conditions and a 40°C/km geothermal gradient) and reducing brine salinity. Maximum
366 sustainable mass injection rate increases with depth mainly because brine vaporization increases
367 with increasing temperature (see Fig. 2 of Spycher and Pruess, 2005). Reducing salinity reduces
368 the amount of permeability loss due to salt precipitation, increases the amount of CO₂ that dis-
369 solves into the brine and increases the amount of water that vaporizes into the CO₂ rich phase,
370 all of which improve injectivity (see Fig. 2 of Spycher and Pruess, 2005). See Mathias et al.
371 (2011b) for a detailed discussion concerning the role of partial miscibility on pressure buildup in
372 this context.

373 Similar to Fig. 8b, Fig. 10 shows plots of PVIR for the scenarios reported in Fig. 9. As in Fig.
374 8b, Figs. 10a and b show PVIR declining with increasing permeability from a maximum value of
375 47%. Furthermore, it is shown that for the small aquifers ($r_E = 5$ km), a minimum PVIR of 6% is
376 reached for permeabilities greater than 100 mD.

377 Fig. 10c shows that for, low permeabilities, there is an increase in PVIR from 47% to 57%

378 with increasing depth (assuming hydrostatic conditions and a 40° C/km geothermal gradient).
 379 This is largely due to the increase in brine vaporization that occurs with increasing temperature.
 380 Fig. 10d shows that for, low permeabilities, there is an increase in PVIR from 44% to 55% with
 381 decreasing salinity. Note that PVIR for the base case but with no permeability reduction due to salt
 382 precipitation are also shown as green circular markers. It can be seen that permeability reduction
 383 has very little effect on PVIR. The increased PVIR with decreasing salinity is again more to do
 384 with changes in brine vaporization.

385 Interestingly, it can be seen that the results presented in Fig. 8b, Fig. 10b and c would collapse
 386 on to a single curve with the correct x-axis translation. Consideration of the inequality ($z_E <$
 387 $0.5615/\alpha$) in Eq. (59) of Mathias et al. (2011b), beyond which the aquifer behaves as a closed
 388 aquifer (also see Mathias et al., 2011a), reveals that an appropriate x-axis variable for the PVIR
 389 plots is the dimensionless time

$$t_D = \frac{2.246kt}{\mu_b \phi (c_r + c_b) r_E^2} \quad (8)$$

390 where k [L^2] is permeability, c_r [$M^{-1}LT^2$] and c_b [$M^{-1}LT^2$] are the rock and brine compressibility,
 391 respectively, and r_E [L] is the radial extent of the aquifer.

392 Fig. 11 shows plots of PVIR against the dimensionless time given in Eq. (8) using the data
 393 previously presented in Figs. 8b, 10a and 10b. Indeed all the data collapses onto a single curve
 394 with PVIR declining from 47% to 6% with increasing t_D . Note, that the decline starts when $t_D = 1$,
 395 which is when enough time has passed for the pressure wave, associated with the CO₂ injection, to
 396 reach the outer boundary of the aquifer (see Mathias et al., 2011a). Once the pressure wave reaches
 397 the outer boundary, pressure buildup proceeds as if in a closed tank. Consequently, compressibility
 398 plays a more important role on injectivity and the importance of relative permeability uncertainty
 399 reduces.

400 7. Summary and conclusions

401 The objective of this study was to explore the possible impact of uncertainty associated with
 402 relative permeability parameters on estimation of injectivity for potential CO₂ storage sites in brine

403 aquifer formations. Pressure buildup due to CO₂ injection into a closed structure was estimated
404 using the semi-analytical solution recently presented by Mathias et al. (2011b). Injectivity was
405 assessed by studying the maximum constant CO₂ injection rate that can be sustained for 30 years
406 without exceeding an injection pressure of 15 MPa, assuming an initial reservoir pressure of 10
407 MPa. A sensitivity analysis on injectivity was undertaken by estimating maximum constant CO₂
408 injection rate for a wide range of permeability, porosity, aquifer extent and reservoir conditions
409 assuming the relative permeability parameter sets (RPPS) (i.e., k_{rg0} , S_{ar} , m , n) for each of 12
410 sandstone cores and 13 carbonate cores obtained from the literature in Table 1 (after Bennion and
411 Bachu, 2008, 2010; Perrin and Benson, 2010; Krevor et al., 2012).

412 Permeability reduction due to salt precipitation was incorporated using a new power law fit to
413 the experimental data recently obtained by Bacci et al. (2011) for a St Bees Sandstone rock core
414 (see Fig. 3).

415 Inspection of the large time component of the semi-analytical solution, previously presented
416 by Mathias et al. (2011b), revealed that the effects of relative permeability can be expressed as
417 a dimensionless constant, P_{rpD} , dependent only on the RPPS and, given an appropriate equation
418 of state, pressure, temperature, brine salinity and permeability reduction due to salt precipitation
419 (recall Eq. (7)). Plots of P_{rpD} against the individual relative permeability parameters (Fig. 4)
420 confirms that although, low end-point relative permeability (k_{rg0}) often leads to low injectivity and
421 a brine exponent (m) close to 1 (i.e. close to linear) often leads to high injectivity, the P_{rpD} is
422 a composite response linked to the combined effects of all four individual relative permeability
423 parameters. Furthermore, plots of P_{rpD} for each of the 25 RPPSs against their corresponding
424 original porosity, permeability and interfacial tensions (IFT) (Figs. 6e, j and o) reveals no apparent
425 link between relative permeability with porosity, permeability, IFT and/or lithology.

426 In the subsequent wider sensitivity looking at RPPS uncertainty in conjunction with other
427 reservoir parameters it was found that variation of injectivity associated with relative permeability
428 parameters was a fraction of that expected due to commonly identified uncertainties associated
429 with permeability and porosity. Nevertheless, the percentage variation in maximum sustainable
430 injection rate (PVIR) associated with the 25 RPPs was as high as $\pm 60\%$ for low permeability
431 aquifers (< 50 mD) or high permeability open aquifers. However, PVIR reduced to $\pm 6\%$ for high

432 permeability closed aquifers (> 100 mD) (see Figs. 8 and 10).

433 Reinspection of the equations presented by Mathias et al. (2011b) led to the realization that
434 PVIR from all the different sensitivity analysis (assuming $P_0 = 10$ MPa, $T = 40^\circ\text{C}$, $w_{sb} = 0.15$)
435 collapsed on to a single curve when the dimensionless time, t_D , given in Eq. (8) is used as the
436 x-axis (see Fig. 11). It was then noticed that for $t_D < 1$, PVIR = 47% and for $t_D > 1$, PVIR
437 gradually declined to 6%. Interestingly, $t_D > 1$ indicates that injection duration has proceeded for
438 sufficiently long such as to allow the pressure wave (associated with injection commencement) to
439 reach the outer boundary of a closed aquifer.

440 It was found that the minimum and maximum injectivities were due to the RPPS of the
441 Tuscaloosa Sandstone and Slave Point Carbonate, respectively. The mean response of the 25
442 RPPS was best by captured by the Eilerslie Sandstone. A linear relative permeability model with
443 $k_{rg0} = 0.1$, $S_{ar} = 0.2$, $m = 1$ and $n = 1$ gives an alternative approximation to the mean response
444 of the 25 RPPS. The latter should be of use to those wishing to benefit from the closed-form
445 expressions for the locations of trailing and leading shocks given by Mathias et al. (2011b).

446 Looking back to Burton et al. (2009)'s finding that uncertainty due to RPPS gave rise to a 4-fold
447 variation in injectivity prediction, the analysis presented in the current article improves on Burton
448 et al. (2009)'s analysis by incorporating an additional 18 RRPSs and additionally accounting for
449 aquifer compressibility. Interestingly, the upper PVIR of $\pm 57\%$, for aquifers where insufficient
450 time has passed for the pressure wave to hit the boundary of the aquifer, corresponds to a 3.7-fold
451 variation. However, the lower limit of $\pm 6\%$ for high permeability closed aquifers corresponds to
452 just a 1.1-fold variation in injectivity. Finally it can be concluded that whilst uncertainty in RRPS
453 can have a substantial effect on injectivity estimation for open aquifers, for closed aquifers, the
454 effects associated with formation compressibility plays a more important role.

455 8. Acknowledgements

456 We would like thank IJGGC reviewer, Andrew Cavanagh, for his many helpful and construc-
457 tive comments. These led to a greatly improved final manuscript. This work was funded by the
458 UK Knowledge Transfer Partnership (KTP) Scheme.

459 **References**

- 460 Allinson, W. G., Y. Cinar, P. R. Neal, J. Kaldi, L. Paterson (2010), CO₂ storage capacity - combining geology, engi-
461 neering and economics, SPE Asia Pacific Oil & Gas Conference and Exhibition, Brisbane, Australia SPE 133804.
- 462 Bacci, G., A. Korre, S. Durucan (2011), Experimental investigation into salt precipitation during CO₂ injection in
463 saline aquifers, *Energy Procedia*, 4, 4450-4456, doi:10.1016/j.egypro.2011.02.399.
- 464 Bachu, S., D. B. Bennion (2008), Effects of in-situ conditions on relative permeability characteristics of CO₂-brine
465 systems, *Environ. Geol.*, 54, 1707-1722, doi:10.1007/s00254-007-0946-9.
- 466 Batzle, M., and Z. Wang (1992), Seismic properties of pore fluids, *Geophysics*, 57, 1396-1408.
- 467 Bennion D. B., S. Bachu (2008), Drainage and imbibition relative permeability relationships for supercritical
468 CO₂/brine and H₂S/brine systems in intergranular sandstone, carbonate, shale, and anhydrite rocks, *SPE Reser-
469 voir Eval. Eng.*, 11, 487-496.
- 470 Bennion D. B., S. Bachu (2010), Drainage and imbibition CO₂/brine relative permeability curves at reservoir condi-
471 tions for carbonate formations, SPE Annual Technical Conference and Exhibition, Florence, Italy, SPE 134028.
- 472 Burton, M., N. Kumar, and S. L. Bryant (2008), Time-dependent injectivity during CO₂ storage in aquifers, SPE/DOE
473 Improved Oil Recovery Symposium, Tulsa, SPE 113937.
- 474 Burton, M., N. Kumar, and S. L. Bryant (2009), CO₂ injectivity into brine aquifers: why relative permeability matters
475 as much as absolute permeability, *Energy Procedia*, 1, 3091-3098, doi:10.1016/j.egypro.2009.02.089.
- 476 Chadwick, R. A., D. J. Noy, and S. Holloway (2009) Flow processes and pressure evolution in aquifers during injection
477 of supercritical CO₂ as a greenhouse gas mitigation measure, *Pet. Geosci.*, 15, 59-73, doi:10.1144/1354-079309-
478 793.
- 479 Dria, D. E., G. A. Pope, and K. Sepehrnoori (1993) Three-Phase Gas/Oil/Brine Relative Permeabilities Measured
480 Under CO₂ Flooding Conditions, *SPE Reservoir Eng.*, 18, 143-150, doi:10.2118/20184-PA.
- 481 Ehlig-Economides, C. A., and M. J. Economides (2010) Sequestering carbon dioxide in a closed underground volume,
482 *J. Pet. Sci. Eng.*, 70, 123-130, doi:10.1016/j.petrol.2009.11.002.
- 483 Fenghour, A., W. A. Wakeham, and V. Vesovic (1998), The viscosity of carbon dioxide, *J. Phys. Chem. Ref. Data*,
484 27, 31-44.
- 485 Georgiadis, A., G. Maitland, J. P. M. Trussler, A. Bismarck (2010), Interfacial tension measurements of the (H₂O +
486 CO₂) system at elevated pressures and temperatures, *J. Chem. Eng. Data*, 55, 4168-4175, doi:10.1021/je100198g.
- 487 Johnson, E. F., D. P. Bossler, V. O. Naumann (1959), Calculation of relative permeability from displace experiments,
488 *Trans. AIME* 216, 370-372.
- 489 Kim, K. Y., W. S. Han, J. Oh, T. Kim, J.-C. Kim (2012), Characteristics of salt-precipitation and the associated pressure
490 build-up during CO₂ storage in saline aquifers, *Transp. Porous Med.* 92, 397-418, doi:10.1007/s11242-011-9909-
491 4.
- 492 Krevor, S. C. M., R. Pini, L. Zuo, S. M. Benson (2012), Relative permeability and trapping of CO₂ and water in

493 sandstone rocks at reservoir conditions, *Water Resour. Res.* 48, W02532, doi:10.1029/2011WR010859.

494 Mathias S. A., P. E. Hardisty, M. R. Trudell, and R. W. Zimmerman (2009), Approximate solutions for pressure
 495 buildup during CO₂ injection in brine aquifers, *Transp. Porous Media*, 79, 265–284, doi:10.1007/s11242-008-
 496 9316-7.

497 Mathias S. A., G. J. Gonzalez Martinez de Miguel, K. E. Thatcher, and R. W. Zimmerman (2011a), Pressure buildup
 498 during CO₂ injection into a closed brine aquifer, *Transp. Porous Media*, In Press, doi:10.1007/s11242-011-9776-z.

499 Mathias S. A., J. G. Gluyas, G. J. Gonzalez Martinez de Miguel, S. A. Hosseini (2011b), Role of partial miscibility
 500 on pressure buildup due to injection of CO₂ into closed and open brine aquifers, *Water Resour. Res.* 47, W12525,
 501 doi:10.1029/2011WR011051.

502 Muller, N. (2011), Supercritical CO₂-brine relative permeability experiments in reservoir rocks literature review and
 503 recommendations, *Transp. Porous Media*, 87, 367–383, doi:10.1007/s11242-010-9689-2.

504 Nordbotten, J. M., M. A. Celia and S. Bachu (2005), Injection and storage of CO₂ in deep saline aquifers: analytic
 505 solution for CO₂ plume evolution during injection, *Transp. Porous Media*, 58, 339–360, doi:10.1007/s11242-004-
 506 0670-9.

507 Okwen, R. T., M. T. Stewart, J. A. Cunningham (2011), Temporal variations in near-wellbore pressures during CO₂
 508 injection in saline aquifers, *Int. J. Greenhouse Gas Control*, In Press, doi:10.1016/j.ijggc.2011.07.011.

509 Orr Jr., F. M. (2007), *Theory of Gas Injection Processes*, Tie-Line Publications, Copenhagen, Denmark.

510 Perrin, J.-C., Benson, S.M. (2010), An experimental study on the influence of sub-core scale heterogeneities on CO₂
 511 distribution in reservoir rocks, *Transp. Porous Media*, 82, 93–109, doi:10.1007/s11242-009-9426-x.

512 Pickup, G., Jin, M., Olden, P, Mackay, E., Sohrabi, M. (2011), A sensitivity study on CO₂ storage in saline aquifers,
 513 SPE EUROPEC/EAGE Annual Conference and Exhibition, Vienna, Austria SPE 143054.

514 Pickup, G., Jin, M., Mackay, E. J. (2012), Simulation of near-well pressure build-up in models of CO₂ injection,
 515 ECMOR XIII 13th European Conference on the Mathematics of Oil Recovery, Biarritz, France, 10-13 September
 516 2012.

517 Pruess, K., C. M. Oldenburg, and G. Moridis (1999), TOUGH2 users guide, version 2.0. Report LBNL-43134,
 518 Lawrence Berkeley National Laboratory, Berkeley, CA, USA.

519 Pruess, K. (2005), ECO2N: A TOUGH2 fluid property module for mixtures of water, NaCl, and CO₂. Report LBNL-
 520 57952, Lawrence Berkeley National Laboratory, Berkeley, CA, USA.

521 Pruess, K. and N. Spycher (2007), ECO2N - A fluid property module for the TOUGH2 code for studies of CO₂ storage
 522 in saline aquifers, *Energy Convers. Manage.*, 48, 1761–1767, doi:10.1016/j.enconman.2007.01.016.

523 Pruess, K. and N. Muller (2009), Formation dry-out from CO₂ injection into saline aquifers: 1. Effects of solids
 524 precipitation and their mitigation, *Water Resour. Res.*, 45, W03402, doi:10.1029/2008WR007101.

525 Sigmund, P. M., F. G. McCaffery (1979), An improved unsteady-state procedure for determining relative-
 526 permeability characteristics of heterogenous porous media, *SPE J.* 19, 15–28, SPE-6720-PA.

527 Spycher, N., K. Pruess and J. Ennis–King (2003), CO₂-H₂O mixtures in the geological sequestration of CO₂. I.
528 Assessment and Calculation of Mutual Solubilities from 12 to 100 °C and up to 600 bar, *Geochim. Cosmochim.*
529 *Acta*, 67, 3015-3031, doi:10.1016/S0016-7037(03)00273-4.

530 Spycher, N. and K. Pruess (2005), CO₂-H₂O mixtures in the geological sequestration of CO₂. II. Partition-
531 ing in chloride brines at 12100 °C and up to 600 bar, *Geochim. Cosmochim. Acta*, 69, 3309-3320,
532 doi:10.1016/j.gca.2005.01.015.

533 van Genuchten, M. Th. (1980), A closed form equation for predicting the hydraulic conductivity of unsaturated soils,
534 *Soil. Sci. Soc. Am. J.*, 44, 892–898.

535 Verma, A., K. Pruess (1989), Thermohydrological conditions and silica redistribution near high-level nuclear wastes
536 emplaced in saturated geological formations, *Water Resour. Res.*, 93, 1159–1173.

537 Wilkinson, M., R.S. Haszeldine, A. Hosa, R. J. Stewart, S. Holloway, M. Bentham, K. Smith, R. Swarbrick, S. Jenkins,
538 J. Gluyas, E. Mackay, G. Smith, S. Daniels, M. Raistrick (2011), Defining simple and comprehensive assessment
539 units for CO₂ storage in saline formations beneath the UK North Sea and continental shelf. *Energy Procedia*, 4,
540 4865–4872. doi:10.1016/j.egypro.2011.02.454.

541 Zeidouni, M., M. Pooladi-Darvish, and D. Keith (2009), Analytical solution to evaluate salt precipitation during CO₂
542 injection in saline aquifers, *Int. J. Greenhouse Gas Control*, 3, 600–611, doi:10.1016/j.ijggc.2009.04.004.

543 Zhou, Q., Birkholzer, J., Tsang, C., Rutqvist, J., 2008. A method for quick assessment of CO₂ storage capacity in
544 closed and semi-closed saline formations. *Int. J. Greenhouse Gas Control* 2 (4), 626–639.

Table 1: Porosity, permeability, IFT and relative permeability parameters (assuming Eqs. (1) and (2)) for the drainage experiments previously presented by Bennion and Bachu (2008, 2010), Perrin and Benson (2010) and Krevor et al. (2012). IFT values for the Bennion and Bachu (2010) results are as reported in Bennion and Bachu (2010). IFT values for the Bennion and Bachu (2008) were obtained from Bachu and Bennion (2008). IFT values for the Perrin and Benson (2010) and Krevor et al. (2012) results were interpolated from values obtained by Georgiadis et al. (2010). Note that for all cores, $k_{rwo} = 1$ and $S_{gc} = 0$.

Unit	Lithology	Source	Porosity (%)	Permeability (mD)	IFT (mN/m)	k_{rg0} (-)	S_{gr} (-)	m (-)	n (-)
Oway	sandstone	Perrin and Benson (2010)	18.2	45	30.0	0.6594	0.4370	2.5	6.5
Berea #1	sandstone	Perrin and Benson (2010)	20.3	430	30.0	0.0700	0.5890	2.5	1.3
Berea #2	sandstone	Krevor et al. (2012)	22.1	914	32.0	0.3948	0.4438	3.2	2.6
Paratte	sandstone	Krevor et al. (2012)	28.3	1156	32.0	0.3284	0.3894	4.6	3.0
Mt. Simon	sandstone	Krevor et al. (2012)	24.4	7.5	32.0	0.4929	0.4371	6.0	1.6
Tuscaloosa	sandstone	Krevor et al. (2012)	23.6	220	32.0	0.0767	0.7030	4.7	3.2
Cardium #1	sandstone	Bennion and Bachu (2008)	15.3	0.356	19.8	0.5260	0.1970	1.3	1.7
Cardium #2	sandstone	Bennion and Bachu (2008)	16.1	21.17	19.8	0.1290	0.4250	1.2	1.3
Viking #1	sandstone	Bennion and Bachu (2008)	12.5	2.7	32.1	0.3319	0.5580	2.9	3.2
Viking #2	sandstone	Bennion and Bachu (2008)	19.5	21.72	32.1	0.2638	0.4230	1.7	2.8
Ellerslie	sandstone	Bennion and Bachu (2008)	12.6	0.376	32.5	0.1156	0.6590	2.1	2.2
Basal Cambrian	sandstone	Bennion and Bachu (2008)	11.7	0.081	27.0	0.5446	0.2940	1.8	5.0
Wabamun #1	carbonate	Bennion and Bachu (2010)	7.9	0.018	29.5	0.5289	0.5950	1.4	5.6
Wabamun #2	carbonate	Bennion and Bachu (2010)	14.8	66.98	29.5	0.1883	0.5690	1.4	2.1
Wabamun #3	carbonate	Bennion and Bachu (2010)	15.4	54.3	29.5	0.1015	0.8520	2.8	5.8
Nisku #1	carbonate	Bennion and Bachu (2010)	9.7	45.92	34.6	0.1768	0.3300	2.8	1.1
Nisku #2	carbonate	Bennion and Bachu (2010)	10.4	21.02	34.6	0.0999	0.4920	2.7	4.6
Nisku #3	carbonate	Bennion and Bachu (2010)	10.9	74.4	34.6	0.1078	0.3970	2.3	2.9
Grosmont	carbonate	Bennion and Bachu (2010)	11.8	153.9	29.5	0.1101	0.5200	1.7	5.2
Morinville Leduc	carbonate	Bennion and Bachu (2010)	11.6	371.9	33.1	0.0746	0.5300	1.8	3.7
Redwater Leduc	carbonate	Bennion and Bachu (2010)	16.8	353.6	35.1	0.0476	0.6650	1.6	4.8
Cooking Lake #1	carbonate	Bennion and Bachu (2010)	9.9	65.3	35.7	0.0685	0.4760	1.4	5.6
Cooking Lake #2	carbonate	Bennion and Bachu (2010)	16.7	4.87	35.7	0.0940	0.5963	1.8	5.4
Slave Point	carbonate	Bennion and Bachu (2010)	9.9	0.217	29.5	0.5037	0.5460	1.6	1.2
Winnipegosis	carbonate	Bennion and Bachu (2010)	14.8	3.09	45.3	0.6117	0.2108	2.4	4.5

Table 2: Parameters used for the TOUGH2 simulations.

Parameter	Symbol	Value
Injection rate,	M_0	= 15 kg/s
Well radius,	r_W	= 0.2 m
Radial extent,	r_E	= 20 km
Porosity,	ϕ	= 0.2
Rock compressibility,	c_r	= $4.5 \times 10^{-10} \text{ Pa}^{-1}$
Initial pressure,	P_0	= 10 MPa
Temperature,	T	= 40 °C
Mass fraction of salt in brine,	ω_{sb}	= 0.15
Residual brine saturation,	S_{ar}	= 0.5
Critical gas saturation,	S_{gc}	= 0.0
End-point relative permeability for brine,	k_{ra0}	= 1.0
End-point relative permeability for CO ₂ ,	k_{rg0}	= 0.3
Permeability reduction factor due to salt precipitation,	k_{rs}	= 1
van Genuchten parameter,	m_v	= 0.46
van Genuchten parameter,	P_{c0}	= 19600 Pa
Formation thickness,	H	= 30 m
Permeability,	k	= 100 mD

Table 3: Base case parameters used for injectivity sensitivity analysis.

Parameter	Symbol	Value
Well radius,	r_W	= 0.2 m
Radial extent,	r_E	= 20 km
Porosity,	ϕ	= 0.2
Rock compressibility,	c_r	= $4.5 \times 10^{-10} \text{ Pa}^{-1}$
Initial pressure,	P_0	= 10 MPa
Temperature,	T	= 40 °C
Mass fraction of salt in brine,	ω_{sb}	= 0.15
Critical gas saturation,	S_{gc}	= 0.0
End-point relative permeability for brine,	k_{ra0}	= 1.0
Permeability reduction factor due to salt precipitation,	k_{rs}	= $(1 - S_s)^{5.74}$
Formation thickness,	H	= 30 m
Permeability,	k	= 100 mD
Injection duration,	t	= 30 years
Maximum pressure,	P_{max}	= $P_0 + 5 \text{ MPa}$
Reference pressure for fluid properties,	P_{ref}	= P_{max}

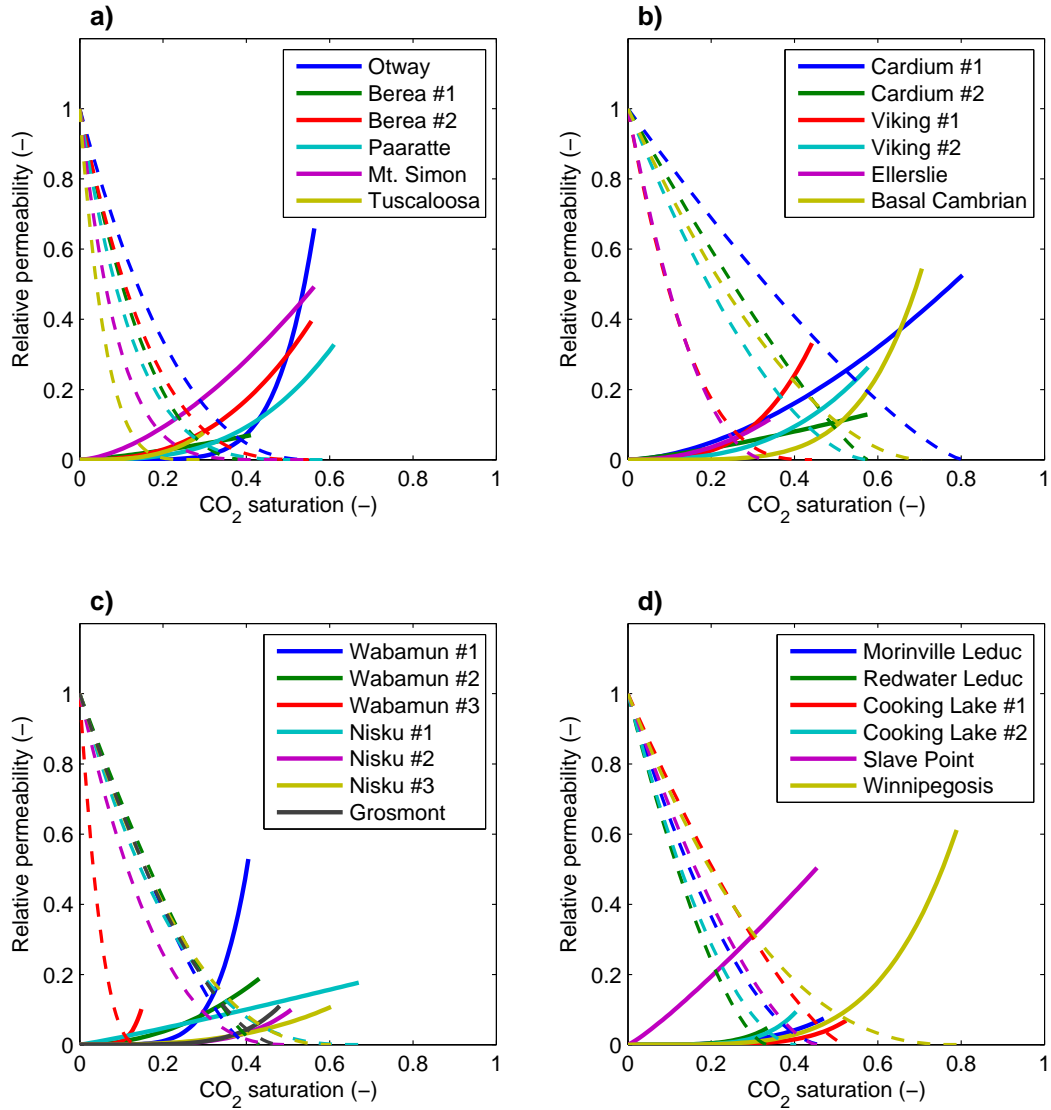


Figure 1: Relative permeability curves constructed using the power law functions in Eqs. (1) and (2) in conjunction with the parameters given in Table 1. Relative permeability for brine and CO₂ are shown as dashed and solid lines, respectively. a) Sandstone cores from Perrin and Benson (2010) and Krevor et al. (2012). b) Sandstone cores from Bennion and Bachu (2008). c) and d) Carbonate cores from Bennion and Bachu (2010).

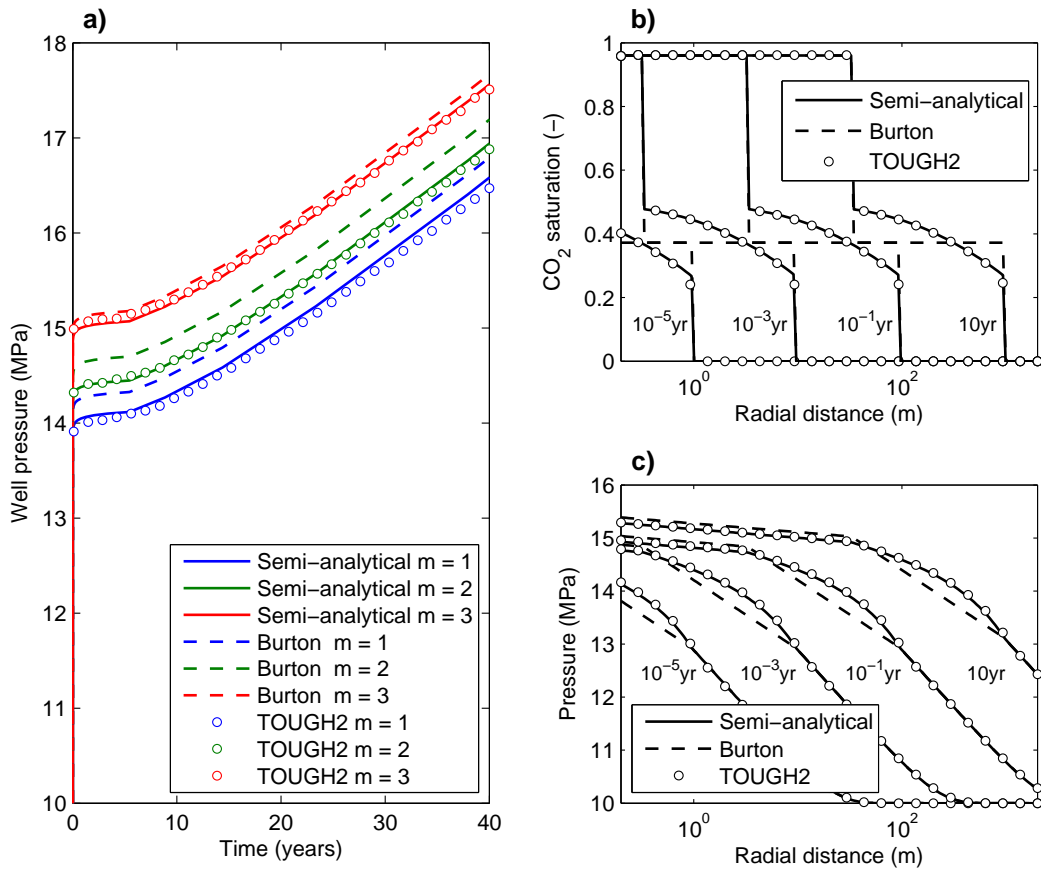


Figure 2: Comparison of the semi-analytical solution (solid lines), the semi-analytical solution with Burton et al. (2008)'s approximation (dashed lines) and TOUGH2 (circular markers). Note that all the simulations presented in this figure assumed n was equal to m . See Table 2 for other parameter values. a) Well pressures with m as indicated. b) CO₂ saturation with $m = 3$ and for times as indicated. c) Reservoir pressures with $m = 3$ and for times as indicated.

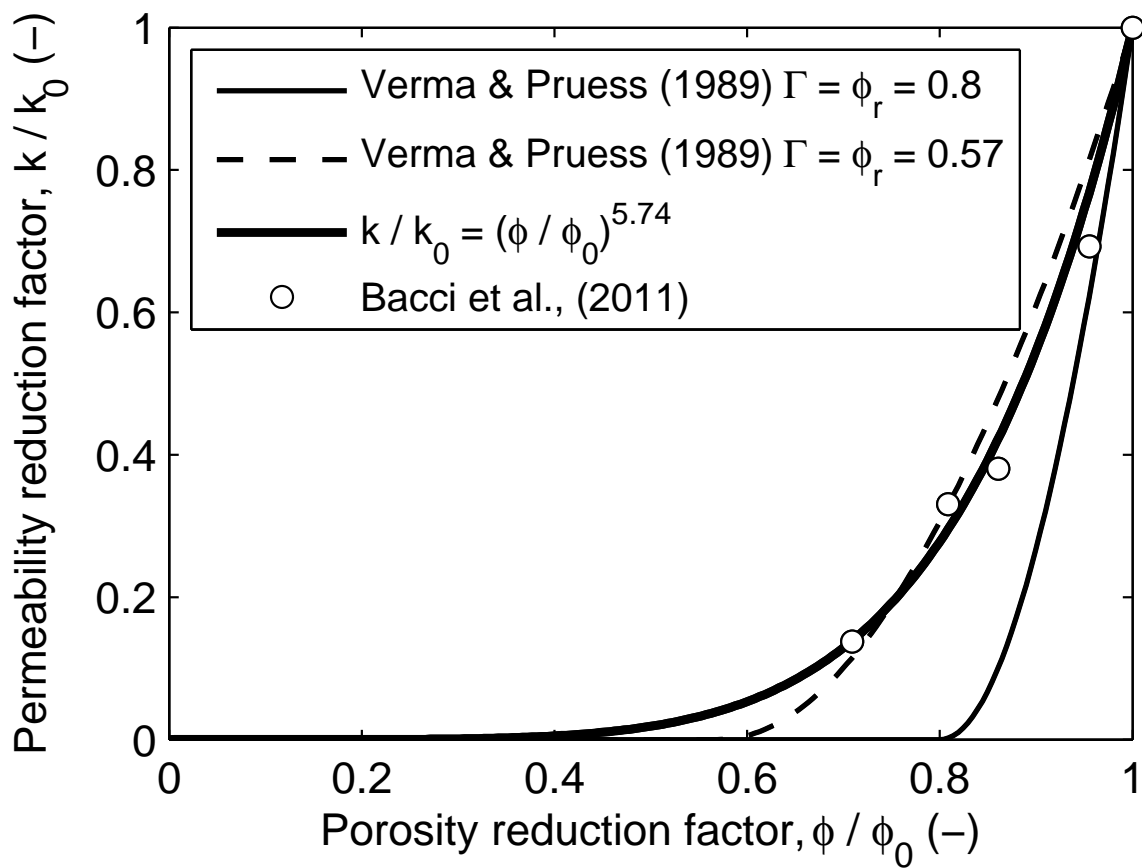


Figure 3: Plot of permeability reduction factor against porosity reduction factor due to salt precipitation. The Verma and Pruess (1989) model is shown with $\Gamma = \phi_r = 0.8$ and $\Gamma = \phi_r = 0.57$. The latter parameter value was obtained by fitting to the experimental data of Bacci et al. (2011), obtained from CO₂ flooding of a St Bees sandstone core. The empirical power law was obtained by linear regression with the experimental data.

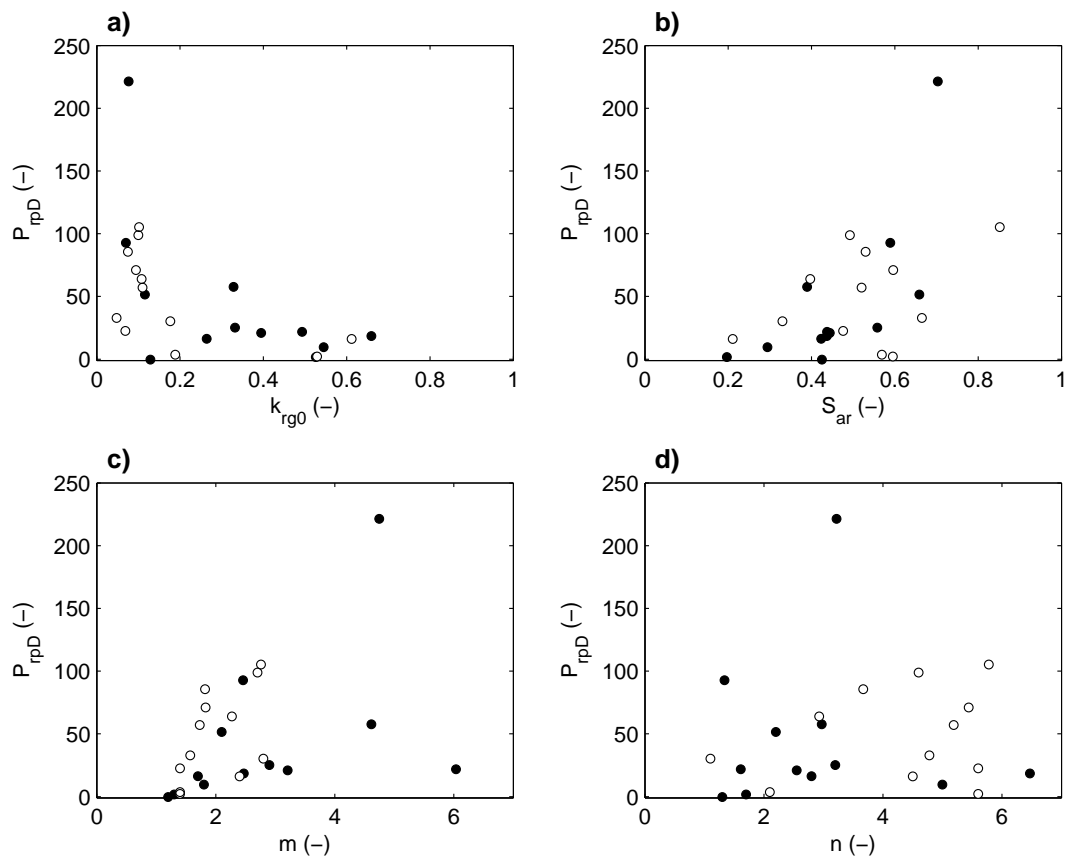


Figure 4: Plot of dimensionless pressure contribution due to relative permeability effects, P_{rpd} , against the four relative permeability parameters for all the relative permeability curves shown in Fig. 1. Closed and open circular markers represent the sandstone and carbonate cores, respectively.

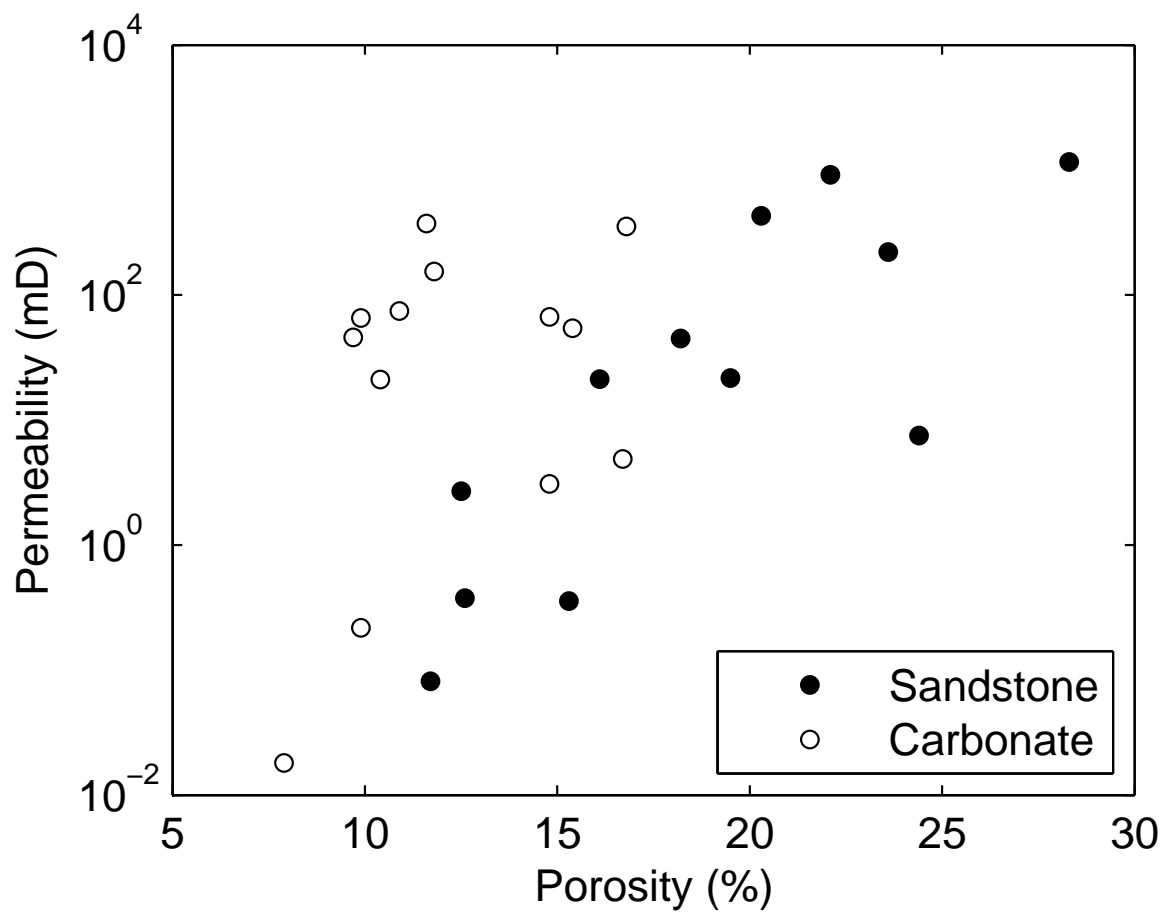


Figure 5: Plot of porosity against permeability for all the cores listed in Table 1. Closed and open circular markers represent the sandstone and carbonate cores, respectively.

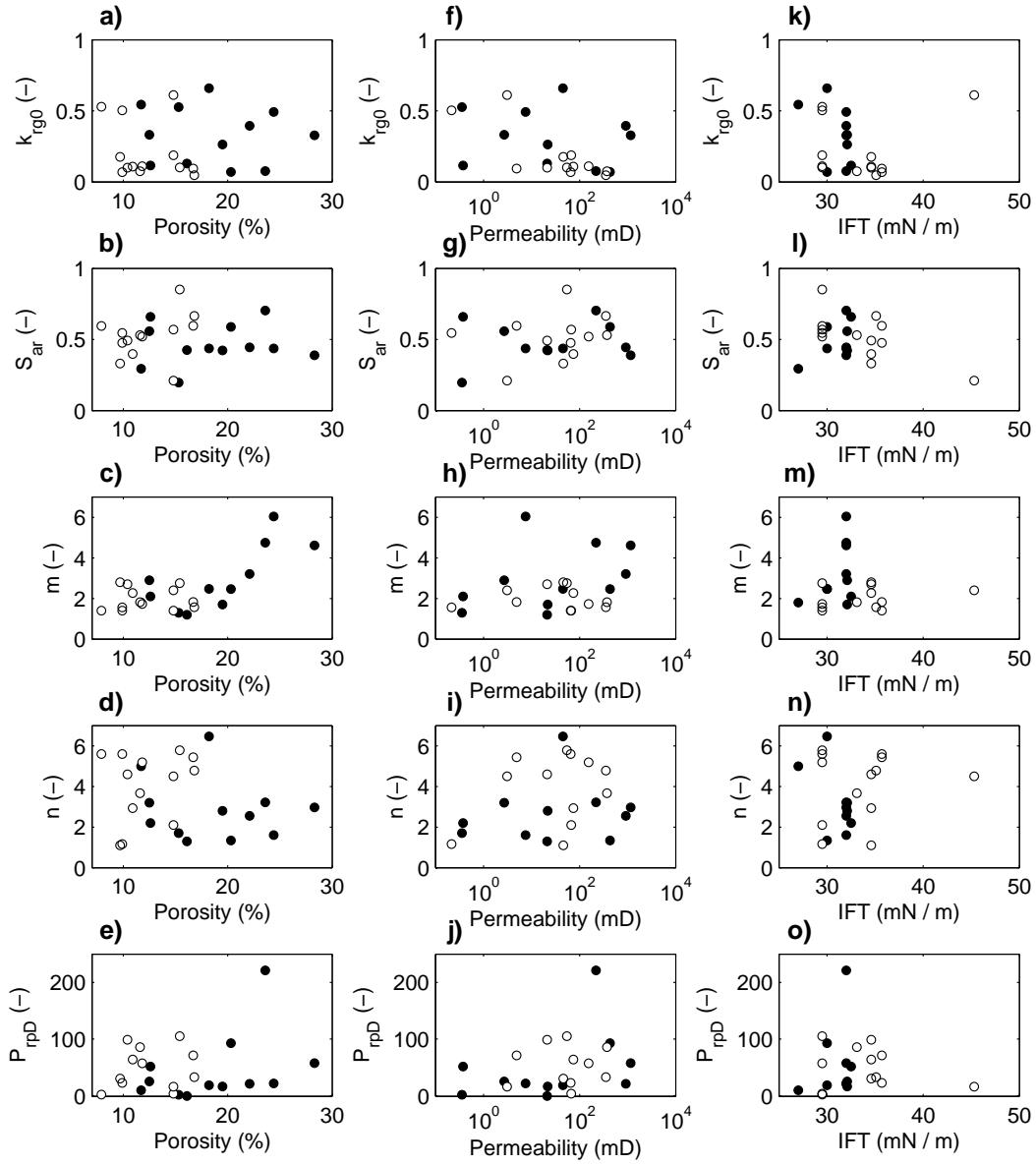


Figure 6: Plots of the four relative permeability parameters and dimensionless pressure contribution due to relative permeability effects, P_{rpb} , for all the cores listed in Table 1, against: a) to e) porosity, f) to j) permeability and k) to o) interfacial tension (IFT). Closed and open circular markers represent the sandstone and carbonate cores, respectively.

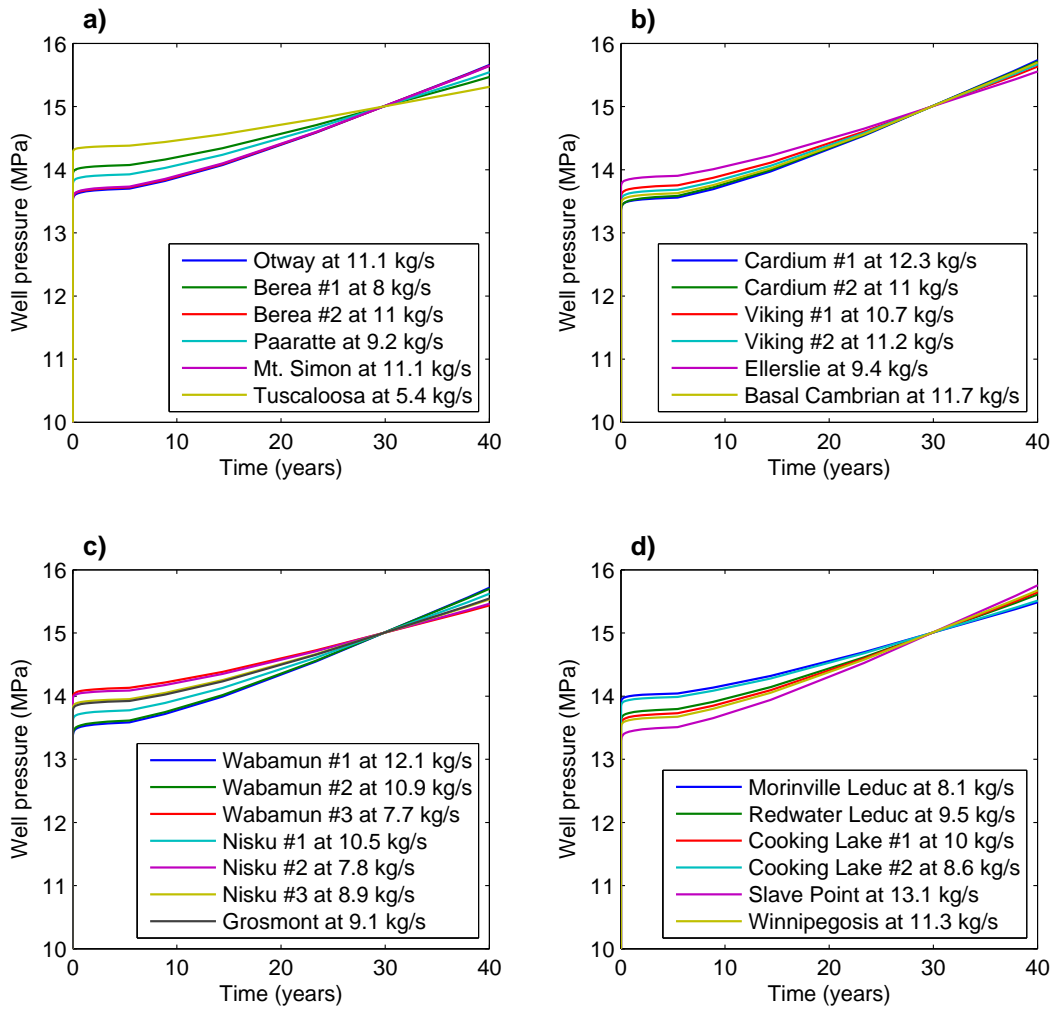


Figure 7: Comparison of simulated well pressures using the 25 different relative permeability parameter sets given in Table 1 and fixing the injection rate such that injection pressure equals 15 MPa after 30 years. See legend for injection rate values. See Table 3 for other parameters. a) Using relative permeability data from the sandstone cores of Perrin and Benson (2010) and Krevor et al. (2012). b) Using relative permeability data from the sandstone cores of Bennion and Bachu (2008). c) and d) Using relative permeability data from the carbonate cores of Bennion and Bachu (2010).

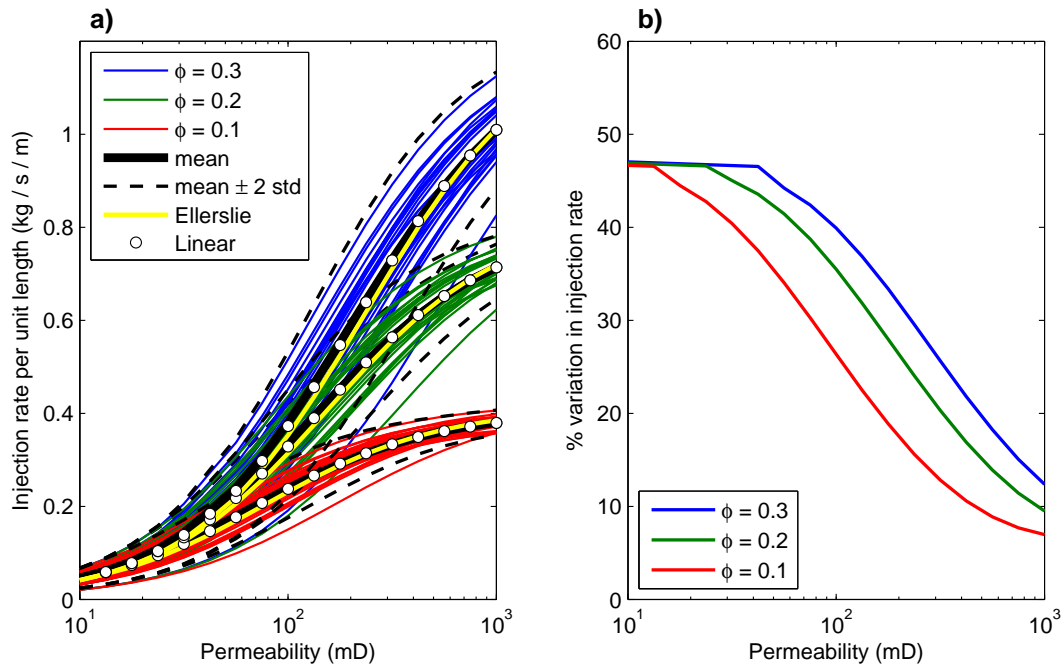


Figure 8: a) Plots of maximum sustainable injection rate per unit length (of fully completed vertical well bore) against permeability for different porosities. The thin solid lines are the results obtained for each of 25 relative permeability parameter sets (from Table 1) but assuming the porosities and permeabilities given by the legend and x-axis, respectively. The black solid and dashed lines represent the mean and the mean \pm two standard deviations (std) of the 25 relative permeability parameter sets (RPPS), respectively. The yellow solid line is due to the individual response of the Ellerslie sandstone RPPS. The white circular markers are results assuming linear relative permeability functions with $k_{rg0} = 0.1$ and $S_{ar} = 0.2$. b) Plots of percentage variation in injection rate (PVIR) (due to the range of responses derived from the 25 RPPS) against permeability for different porosities (obtained by dividing two standard deviations by the mean and multiplying by 100).

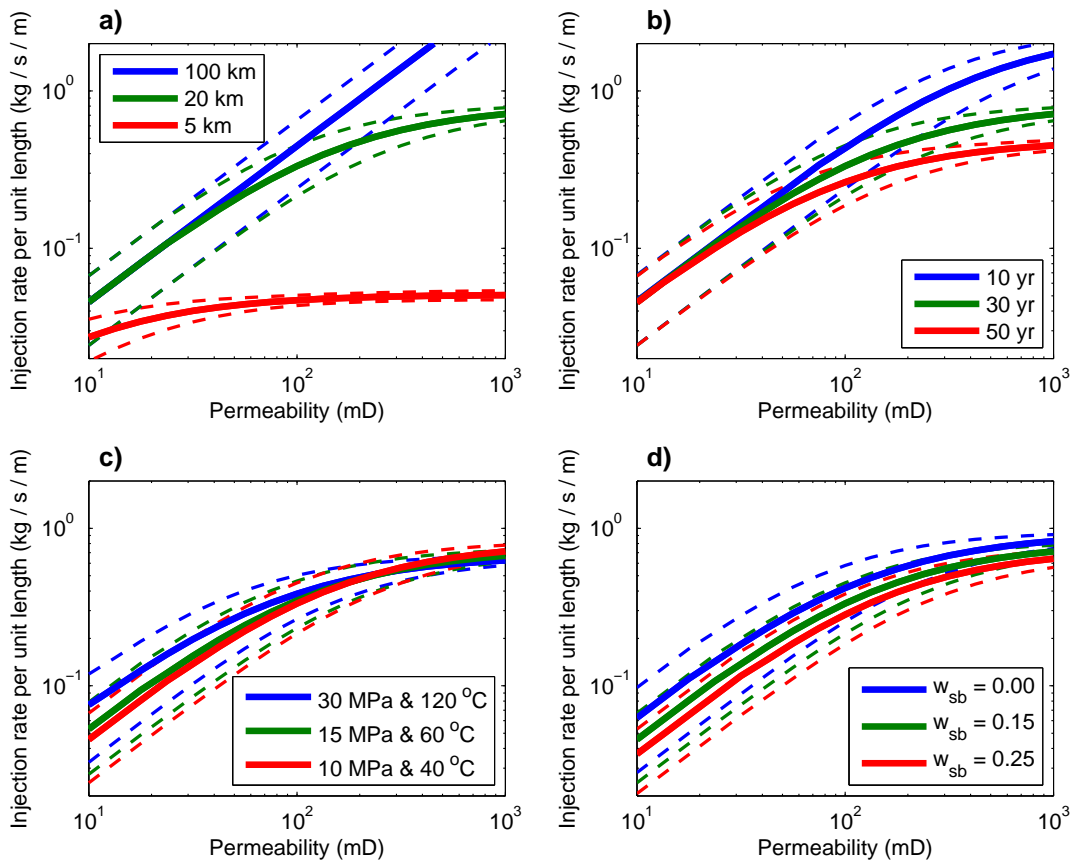


Figure 9: Similar to Fig. 8a but looking at: a) variation in radial extent of aquifer (r_E); b) variation in injection duration; c) variation in aquifer conditions; d) variation in formation water salt mass fraction (w_{sb}). The solid and dashed lines represent the mean and the mean \pm two standard deviations (std) of the 25 RPPS, respectively.

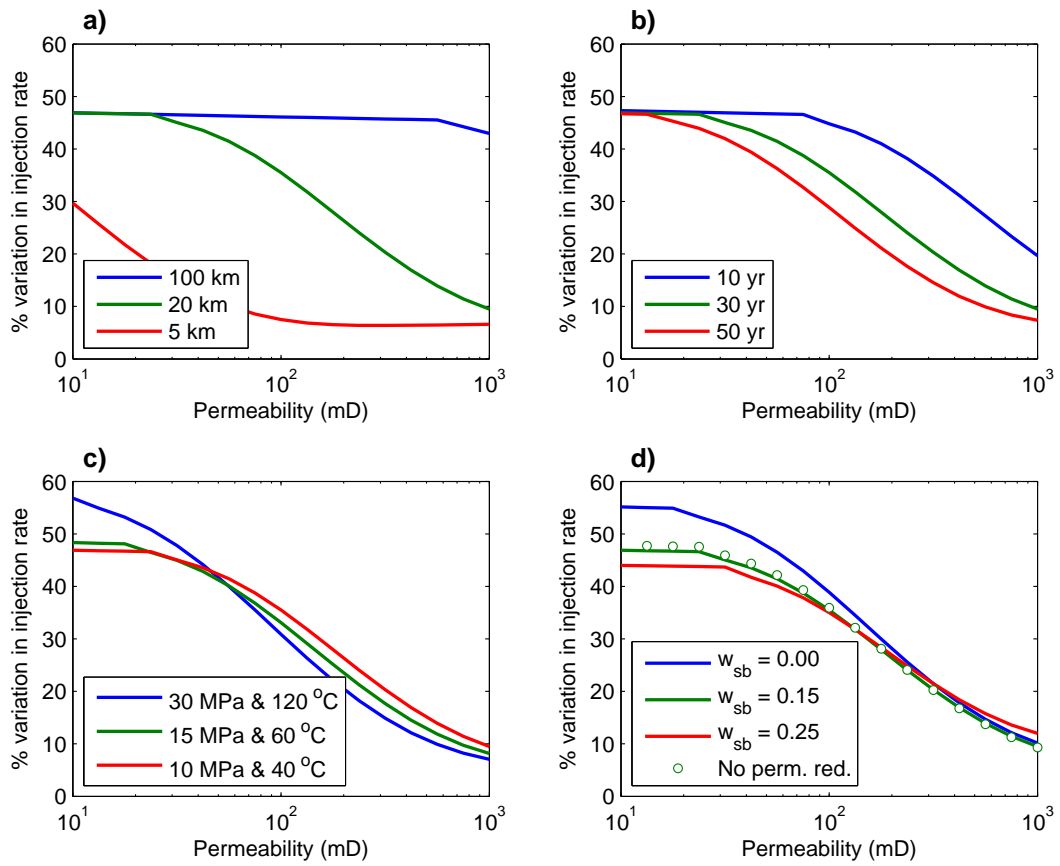


Figure 10: The same as Fig. 8b but looking at: a) variation in radial extent of aquifer (r_E); b) variation in injection duration; c) variation in reservoir conditions; d) variation in formation water salt mass fraction (w_{sb}).

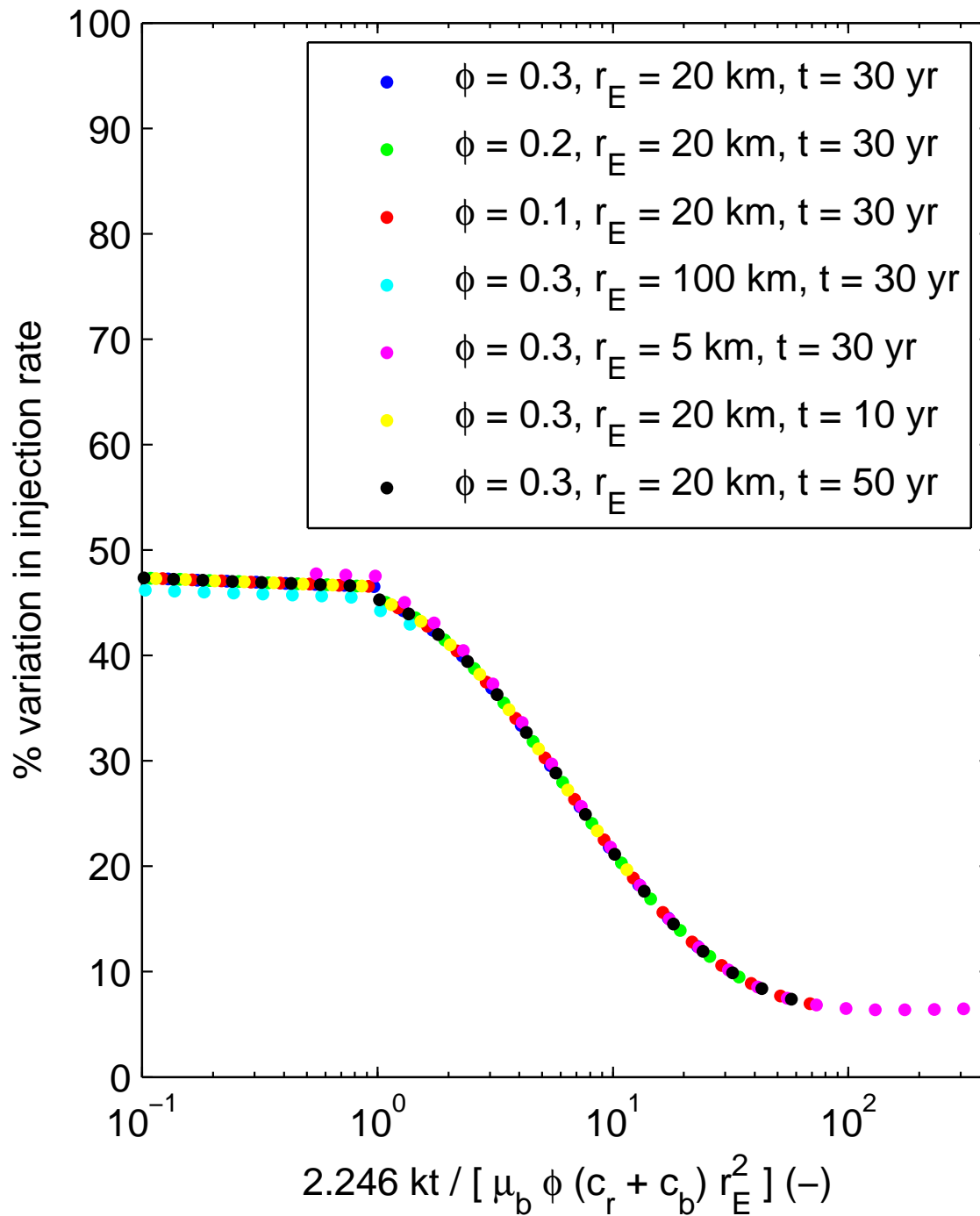


Figure 11: Plots of PVIR against dimensionless time, combining all the data previously presented in Figs. 8b, 10a and 10b.